

Ultrasonic liquid metal processing: The essential role of cavitation bubbles in controlling acoustic streaming

G.S. Bruno Lebon^{1,2*}, Iakovos Tzanakis^{3,5}, Koulis Pericleous², Dmitry Eskin^{1,4}, Patrick S. Grant⁵

¹Brunel Centre for Advanced Solidification Technology (BCAST), Brunel University London, Uxbridge UB8 3PH, United Kingdom

²Computational Science and Engineering Group (CSEG), Department of Mathematics, University of Greenwich, London SE10 9LS, United Kingdom

³Faculty of Technology, Design and Environment, Oxford Brookes University, Oxford OX33 1HX, United Kingdom

⁴Tomsk State University, Tomsk 634050, Russia

⁵Department of Materials, University of Oxford, Oxford, OX1 3PH, United Kingdom

*Corresponding author. Email address: Bruno.Lebon@brunel.ac.uk

Abstract

The acoustic streaming behaviour below an ultrasonic sonotrode in water was predicted by numerical simulation and validated by experimental studies. The flow was calculated by solving the transient Reynolds-Averaged Navier-Stokes equations with a source term representing ultrasonic excitation implemented from the predictions of a nonlinear acoustic model. Comparisons with the measured flow field from Particle Image Velocimetry (PIV) water experiments revealed good agreement in both velocity magnitude and direction at two power settings, supporting the validity of the model for acoustic streaming in the presence of cavitating bubbles. Turbulent features measured by PIV were also recovered by the model. The model was then applied to the technologically important area of ultrasonic treatment of liquid aluminium, to achieve the prediction of acoustic streaming for the very first time that accounts for nonlinear pressure propagation in the presence of acoustic cavitation in the melt. Simulations show a strong dependence of the acoustic streaming flow direction on the cavitating bubble volume fraction, reflecting PIV observations. This has implications for the technological use of ultrasound in liquid metal processing.

Keywords: acoustic streaming; acoustic cavitation; nonlinear acoustics; modelling; aluminium, particle image velocimetry

Introduction

The complexity of non-linear acoustics and cavitation phenomena, the opaqueness, high temperatures and chemical reactivity of metallic melts hinder the study of ultrasonic melt processing. To improve the understanding of ultrasonic process effects on liquid metals, an

extensive research program was undertaken over the past five years [1] to implement a numerical model that can realistically predict acoustic pressures and acoustic streaming in the melt in the presence of cavitation, and to validate the model experimentally.

Processing melts with ultrasound improves physical and mechanical properties of the treated metallic materials [2–4]. These beneficial effects of ultrasonic melt processing are attributed to acoustic cavitation and acoustic streaming before, and during, the solidification of the liquid metal [5]. While this technology has been successfully applied in the laboratory and at the pilot plant scale, further up-scaling requires multiple ultrasonic sources, which undermines the economic attraction, and imposes technological restrictions on widespread industrial adoption. To up-scale ultrasonic melt processing to the industrial scale effectively, there is a need to bridge the gap between understanding of ultrasonic fundamentals and the interaction between cavitation and larger-scale melt flow, with the aim of operating the ultrasound devices in a manner that minimises the number of ultrasonic sources while simultaneously maximising the volume of effectively treated melt [6].

Quantifying recirculation patterns and mass exchange between the cavitation zone and the rest of the melt bulk is crucial for understanding how to optimize ultrasonic melt processing because this effectively determines the treated volume. Recirculation of the liquid melt, over length scales that are matched to the dimensions of the melt volume, will also help to reduce temperature gradients in the melt, thereby promoting a preferred equiaxed grain structure [7]. In the direct-chill (DC) casting process that is used widely in the aluminium industry, acoustic streaming promotes forced convection which has been shown to decrease macrosegregation and to promote solid fragmentation and thus self-grain refinement [4,8]. Other beneficial effects include deagglomeration and wetting of inclusions [9], and their dispersion that increases the number of substrates available for heterogeneous nucleation of the solid, thereby promoting grain refinement.

Numerical models describing the dynamics of acoustic cavitation can synthesize existing empirical knowledge and provide a framework for understanding the complex mechanisms involved. Accurate prediction of acoustic streaming is however plagued by difficulties, especially the challenges in modelling nonlinear acoustic pressure propagation [10]. Therefore, it is not surprising that a model of acoustic streaming in the presence of acoustic cavitation has only recently appeared in the literature [11]. Earlier attempts of modelling acoustic cavitation and flows in liquid metals [12] were limited due to the use of a homogeneous cavitation model [13] that is only applicable to liquids containing vapour bubbles [11]. More accurate efforts in quantifying acoustic pressures in liquid aluminium [14,15] employ non-linear equations as suggested by van Wijngaarden [16] following previous successful implementation in water [17,18]. However, these models are computationally expensive, as the dynamics of bubbles in each computational cell have to be resolved [10,15]. Incorporating bubble motion in such models [19] results in additional computational complexity.

From the experimental perspective, there are relatively few quantitative studies on acoustic cavitation and streaming during ultrasonic processing. Acoustic streaming is known to form a conical or jet flow pattern, depending on the input acoustic power, with recirculating flows influencing the entrainment of bulk liquid and small solid inclusions back into the cavitation zone [20–22]. Using Particle Image Velocimetry (PIV) experiments in low temperature liquids (mostly water) and high-speed synchrotron X-ray radiography experiments, many groups have attempted to visualise and understand what is happening inside the cavitation zone of a liquid melt. Feng *et al.*

[23] described the mechanisms of microstructural refinement based on real time acoustic flow observations of a sonicated Al-35Cu alloy melt. Mirihanage *et al.* [24] reported the flow velocity of the acoustic streaming by observing the bubble streamlines and local turbulent fluctuations of an Al-Cu metal matrix nano-composite melt. Bing *et al.* [25] investigated the effect of acoustic flow on the liquid-solid interface of a Bi-8%Zn alloy using X-ray radiography and image analysis: a toroidal flow pattern was observed, coaxial with the sonotrode, appearing in 2D as a clockwise vortex on the left and a counter-clockwise vortex on the right. The recorded velocities were in the range of 0.5–0.6 ms⁻¹. Overall, there remains a lack of a generic, validated approach that can describe behaviour across a range of conditions, materials and geometries that can guide industrial practise, with the ultimate goal of ultrasonic treatment implementation in casting processes.

Recent progress in the theory on non-linear sound propagation [26–29] resulted in an easier-to-solve nonlinear Helmholtz equation to quantify the acoustic pressure field. Louisnard extended his nonlinear model to account for acoustic streaming in the presence of cavitation with two-dimensional results comparing well with experiment [11]. In this paper, this acoustic streaming model is adapted to a finite volume computational fluid dynamics solver compiled in OpenFOAM [30] to predict the flow below the sonotrode in both water and liquid aluminium. The model is compared with PIV measurements in water sonicated at two different acoustic powers. Water is used for comparison, because it is deemed a suitable physical analogue to aluminium for studying ultrasonic melt processing [31]. The model is then applied to aluminium to predict the acoustic streaming pattern at different transducer powers and the likely implications for liquid metal processing are discussed.

Theory

Acoustic field model

The Caflisch equations describe acoustic propagation in a bubbly liquid represented as a continuous medium [17]. Following conservation of mass and momentum, we obtain

$$\frac{1}{\rho c^2} \frac{\partial p_a}{\partial t} + \nabla \cdot \mathbf{u} = \frac{\partial \alpha}{\partial t}, \quad (1)$$

$$\rho \frac{\partial \mathbf{u}}{\partial t} + \nabla p_a = 0, \quad (2)$$

where ρ is the (pure) liquid density, c is the speed of sound, p_a is the acoustic pressure, \mathbf{u} is the velocity, and α is the bubble volume fraction given by

$$\alpha = \frac{4}{3} \pi R^3 N = VN, \quad (3)$$

where R is the bubble radius, $V = \frac{4}{3} \pi R^3$ is the bubble volume, and N is the bubble density (number of bubbles per unit volume). To complete the Caflisch model, the Rayleigh-Plesset equation [32,33] describes the bubble dynamics

$$\rho R \ddot{R} + \frac{3}{2} \rho \dot{R}^2 = p_b + p_v - \frac{2\sigma}{R} - \frac{4\mu \dot{R}}{R} - p_0 + p_A \sin(\omega t), \quad (4)$$

where the bubble pressure is given by $p_b = p_{g,0} \left(\frac{R_0}{R}\right)^{3\kappa}$ with $p_{g,0}$ being the gas pressure at the equilibrium radius R_0 . Assuming an adiabatic gas, the polytropic exponent $\kappa = 1.4$, p_v is the vapour pressure, σ is the interfacial tension between the gas and the liquid, μ is the dynamic viscosity of the liquid, p_0 is the pressure at infinity (set to atmospheric pressure) and p_A is the pressure amplitude due to the excitation source whose angular frequency is $\omega = 2\pi f$.

During rapid pulsation, a cavitating bubble undergoes rapid changes in pressure p_b and temperature. Heat transfer between the gas and liquid during these pulsations results in energy dissipation. A nonlinear model can be obtained by taking into account gas continuity and energy conservation without explicitly solving for them [26,28,34]. We follow Louisnard's approach [26] to obtain the following dissipation functions:

$$\Pi_{th} = \frac{1}{T} \int_0^T -p_b \frac{\partial V}{\partial t} dt, \quad (5)$$

$$\Pi_v = \frac{1}{T} \int_0^T 16\pi\mu R \dot{R}^2 dt, \quad (6)$$

where $T = \frac{1}{f}$ is one period, Π_{th} is the period-averaged heat loss from the bubble and Π_v is the period-averaged dissipation by viscous friction.

Denoting the harmonic part of p_a as $\Re(Pe^{i\omega t})$, the complex amplitude P approximately fulfils the nonlinear Helmholtz equation [26,27]

$$\nabla^2 P + K^2 P = 0, \quad (7)$$

where the real and imaginary parts of K^2 are given by

$$\Re(K^2) = \frac{\omega^2}{c^2} + \frac{4\pi R_0 \omega^2 N}{\omega_0^2 - \omega^2}, \quad (8)$$

$$\Im(K^2) = -2\rho\omega N \frac{\Pi_{th} + \Pi_v}{|P|^2}. \quad (9)$$

The resonant frequency ω_0 is given by [34,35]

$$\omega_0 = \sqrt{\frac{p_0}{\rho R_0^2} [(1+S)\Re(\Phi) - S]}, \quad (10)$$

where $S = \frac{2\sigma}{p_0 R_0}$, $\Phi = \frac{3\kappa}{1-3(\kappa-1)i\chi[\sqrt{i\chi} \coth \sqrt{i\chi-1}]}$, $\chi = D/\omega R_0^2$ and D is the gas diffusivity.

The bubble density is assumed to follow the step function [26]

$$N = \begin{cases} N_0 & \text{if } |P| > P_B \\ 0 & \text{if } |P| \leq P_B \end{cases}. \quad (11)$$

Where the Blake threshold is $P_B = p_0 \left[1 + \sqrt{\frac{4}{27} \frac{S^3}{1+S}}\right]$.

Note that the bubble fraction is not explicitly computed in this model. Instead, the acoustic pressure is estimated by solving equation (7), from which the acoustic streaming force can be inferred. Also,

the model is concerned with the ultrasonic processing of light alloy melts or analogues, and not in simulating the different process of bubble entrainment (e.g. due to degassing). Therefore, the current model only considers the effect of internally generated cavitation bubbles.

Fluid flow model

Fluid flow is modelled using the incompressible Reynolds-Averaged Navier-Stokes (RANS) equations closed with the k - ω shear stress transport model [36]:

$$\nabla \cdot \mathbf{u} = 0, \quad (12)$$

$$\frac{\partial \mathbf{u}}{\partial t} + \nabla \cdot (\mathbf{u} \otimes \mathbf{u}) = \nu \nabla^2 \mathbf{u} - \frac{\nabla p}{\rho} + \mathbf{f}, \quad (13)$$

where p is the flow pressure, $\nu = \mu/\rho$ is the kinematic viscosity, and \mathbf{f} represents the force driving acoustic streaming.

$$\mathbf{f} = -\nabla(\overline{\mathbf{v} \otimes \mathbf{v}}), \quad (14)$$

where $\mathbf{v} = \frac{\nabla p}{\rho \omega}$ is the acoustic streaming velocity [11]. The overbar indicates that the values are obtained from averaging over a period of the acoustic bubble (specifically in the calculation of Π_{th} and Π_v).

$$\frac{\partial k}{\partial t} + \nabla \cdot (\mathbf{u}k) = \nabla \cdot (D_k \nabla k) + G - \frac{2}{3}k(\nabla \cdot \mathbf{u}) - \beta^* \omega k + S_k, \quad (15)$$

$$\frac{\partial \omega_t}{\partial t} + \nabla \cdot (\mathbf{u}\omega_t) = \nabla \cdot (D_\omega \nabla \omega_t) + \frac{\gamma G}{\nu} - \frac{2}{3}\gamma \omega_t(\nabla \cdot \mathbf{u}) - \beta \omega_t^2 - (F_1 - 1)CD_{k\omega} + S_\omega. \quad (16)$$

The turbulent viscosity is given by

$$\mu_t = a_1 \frac{\rho k}{\max(a_1 \omega_t, b_1 F_{23} S)}. \quad (17)$$

Experimental validation

Geometry

The physical arrangement corresponds to the experimental configuration of particle image velocimetry (PIV) experiment in a water tank, illustrated in Figure 1. A 20 kHz transducer (Hielscher UP1000) sonicated water in a rectangular glass tank of base area 300 mm × 200 mm with water height 150 mm. The cylindrical sonotrode with a diameter 40 mm was immersed 20 mm below the water surface. Two conditions were considered: when the transducer was operating at 50 % power corresponding to a null-peak amplitude of 4.25 μm , and 100% power corresponding to an amplitude of 8.5 μm .

A TSI (USA) PIV system measured velocities in the plane of a narrow two-dimensional 10 mm × 10 mm laser-illuminated light sheet, or “window”, using multiple, serial double short Nd-YAG laser flashes with “frozen” images of the flow filled with glass hollow sphere seeded particles (~10 μm in diameter) recorded perpendicular to the light sheet at a rate of 5 pair of images per second. Image pairs were then analysed using TSI software to retrieve 2D velocity vector maps which were time averaged over typically 100 pairs. Further details of the PIV arrangement can be found elsewhere

[37].

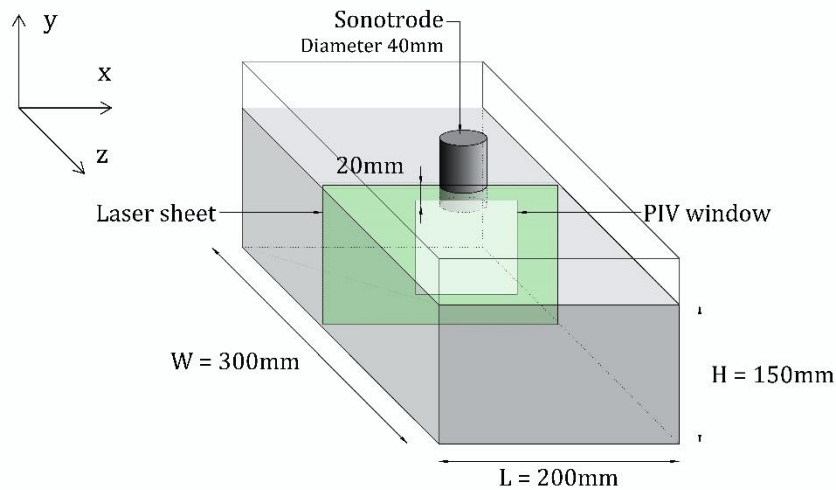


Figure 1. Schematic of water tank for PIV measurements. The sonotrode is immersed 20 mm below the free surface of water at the axis of tank. Velocities are measured in a 2D 10 mm \times 10 mm window below the sonotrode.

Numerical implementation

The numerical simulations are performed in a modified version of the solver *pisoFoam* of the open source library OpenFOAM version 4.x. Table 1 lists the material properties that are used to solve the Rayleigh-Plesset equation (4) and the coupled acoustic-flow equations (7) and (12–13, 15–16).

Table 1. Transport properties and material properties for water and aluminium [4].

Initial bubble radius R_0 (μm)	5	
Gas diffusivity D ($\text{m}^2 \text{s}^{-1}$)	1.7e-4	
Equilibrium pressure p_0 (Pa)	101325.0	
Polytropic coefficient κ	1.4	
Material properties	Water	Aluminium
Density ρ (kg m^{-3})	1000	2375
Speed of sound c (m s^{-1})	1482.0	4600.0
Kinematic viscosity ν ($\text{m}^2 \text{s}^{-1}$)	1.004e-6	5.5e-7
Surface tension σ with air (N m^{-1})	0.079	0.86
Vapour pressure p_v (MPa)	0.0022	0.0

Table 2 lists the discretization schemes and solver control parameters for the simulations. A summary of the solver algorithm is detailed below:

1. The Rayleigh-Plesset equation is solved for a bubble of equilibrium radius R_0 for a range of pressures which include the pressure below the sonotrode at the operating power. This pressure is estimated from measurements in similar experiments using a calibrated cavitometer [38].

2. The values of Π_{th} and Π_v at the operating pressure are obtained from the integrals (5–6) over a period of oscillation.

The following steps are looped over the run time. Even if steady state is expected at very low bubble volume fractions, solving transient equations adds more stability due to the transient term acting as an inertial relaxation term in the flow equations.

3. For each time step, the harmonic component of the acoustic pressure equation (7) is solved as follows:

- a. Equation (7) is split into two equations for the real and imaginary parts of P .

$$\nabla^2 \Re(P) + \Re(K^2) \Re(P) = \Im(K^2) \Im(P) \quad (18)$$

$$\nabla^2 \Im(P) + \Re(K^2) \Im(P) = -\Im(K^2) \Re(P) \quad (19)$$

- b. Equations (18) and (19) are solved sequentially using the finite volume method. Note that convergence is achieved only with a suitable use of preconditioners for both equations, i.e. Simplified Diagonal-based Incomplete Cholesky preconditioner (DIC) with DIC smoothing followed by Gauss-Seidel (DICGaussSeidel).
- c. The computed values of acoustic pressure are used in the source term (14)
4. If activated, the momentum equations (13) are solved in the momentum predictor step.
5. Pressure and velocity are solved for using the Pressure-Implicit Splitting of Operators (PISO) algorithm [39].
6. The turbulence model is solved during the last stage of the time loop.

Table 2: OpenFOAM discretization schemes and solver control parameters.

Discretization schemes	
ddtSchemes	Euler
gradSchemes	
Default	Gauss linear
grad(u)	cellLimited Gauss linear 1
divSchemes	
Default	Gauss linear
div(ϕ , \mathbf{u})	bounded Gauss linearUpwind limited
div(ϕ , k), div(ϕ , ω_t)	Gauss limitedLinear 1
laplacianSchemes	
Default	Gauss linear corrected
interpolationSchemes	
Default	linear
snGradSchemes	
Default	corrected
Solver control parameters	
P	GAMG

U, k, ω_t	smoothSolver, symGaussSeidel
$\mathfrak{R}(P) \mathfrak{S}(P)$	PCG, DILU Preconditioner DIC, DICGaussSeidel with cacheAgglomeration
momentumPredictor	no
nCorrectors	2
nNonOrthogonalCorrectors	1
pRefCell	0
pRefValue	p_0/ρ

Figure 2 and Table 3 show the boundary conditions of the simulation. The surfaces of the tank are rigid walls at which the no-slip condition is imposed. The free surface is modelled as a surface of constant pressure. The pressure at the sonotrode is prescribed by specifying the expected pressure normal gradient as specified in Table 3 [28]. The pressure below the sonotrode was indirectly prescribed by fixing the pressure gradient at the surface as $\omega \rho v_n = \omega^2 \rho y$. The walls of the sonotrode were presumed to be rigid walls.

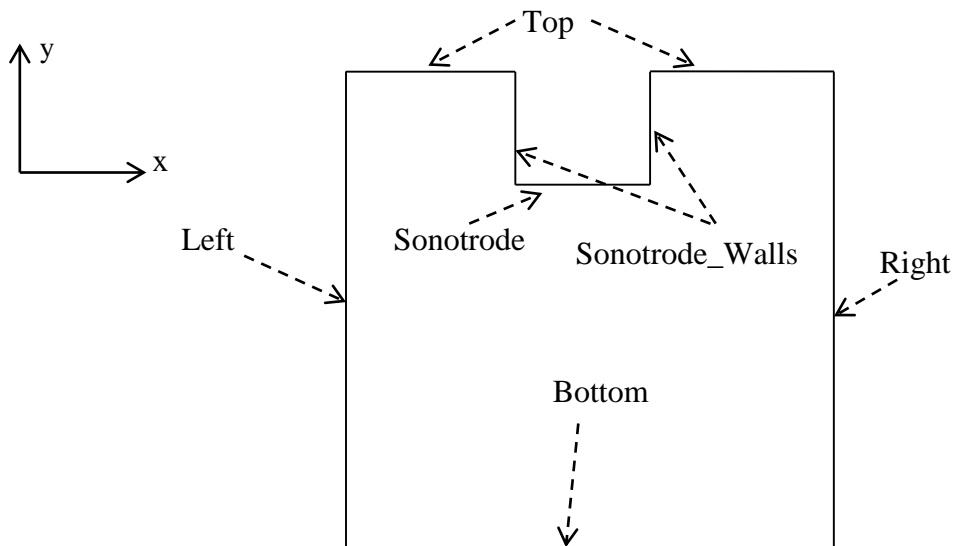


Figure 2. Boundary conditions for 2D model.

Table 3: Boundary conditions

	\mathbf{u}	p	k, ω_t, v_t	$\mathfrak{R}(P) \mathfrak{S}(P)$
Top	No slip	Normal gradient = 0 Pa m^{-1}	$kqRWallFunction$ (zero gradient boundary condition), ω wall function [40], $nutkWallFunction$ (turbulent kinematic viscosity condition when using wall functions, calculated from turbulent kinetic energy) [30]	Fixed value = 0 Pa
Sonotrode_walls, Bottom, Left, Right				Normal gradient = 0 Pa m^{-1}
Sonotrode				Fixed gradient = $\omega \rho v_n = \omega^2 \rho y$

Results and Discussion

Application of the acoustic streaming model to water

The numerical model was solved in the two-dimensional plane of the laser sheet shown in Figure 1. Comparison with experiment was principally qualitative as a full three-dimensional simulation is required for quantitative comparison, which is the focus of further work, together with the use of large-eddy simulations (LES) to model turbulence more accurately [41,42]. Nevertheless, a qualitative comparison is helpful to understand, for example, a surprising upward flow in PIV experiments at low power, as shown in Figure 3 (a). At 50 % of the maximum sonotrode power, the net average flow along the axis of the sonotrode was upwards, with recirculation patterns around the axis. At full power, the acoustic streaming forces the liquid at high speed towards the bottom of the tank (which is the streaming pattern usually reported).

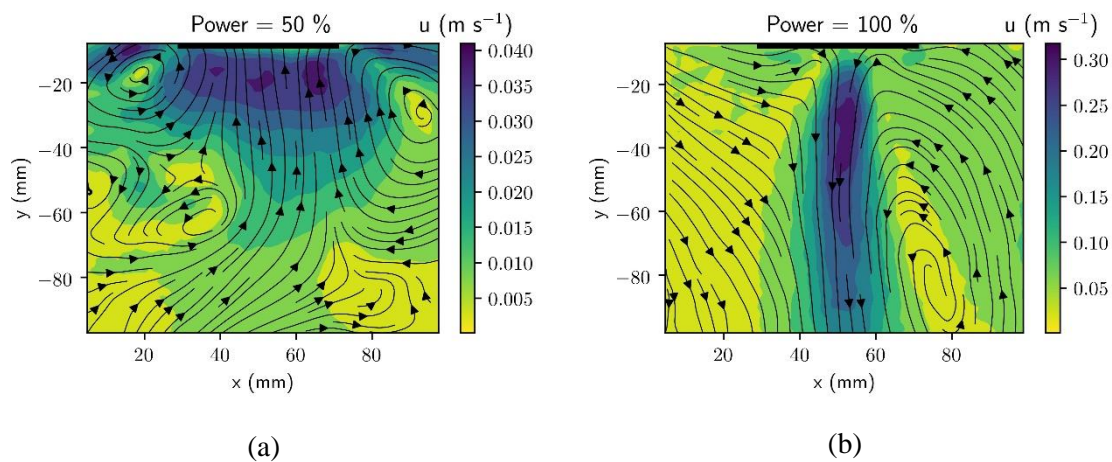


Figure 3: Typical time averaged images of PIV showing spatial distribution of average acoustic flow structures under different input power at 50% (a) and 100% (b) acoustic power from the transducer [37]. The colours represent velocity magnitude in m s^{-1} . The streamlines show the direction of the flow and recirculations. The thick line at the top represents the sonotrode surface.

Acoustic streaming pattern at 50 % power

Figure 4 shows the recording of the flow field with the PIV at 2 s intervals. These 6 snapshots are among the 100 vector file recordings used to calculate the average flow pattern presented in Figure 3 (a). The flow is always upwards. Note that, while the sonotrode is oscillating up and down, the fluid below the sonotrode surface will also be pushed upwards and downwards with the forcing frequency of the sonotrode. However, the resolution of the PIV equipment cannot capture this fast instantaneous motion and what is recorded is the net average flow. This net average flow is of particular significance in ultrasonic melt processing where ultrasound is continuously fed into the melt for time frames of the order of minutes.

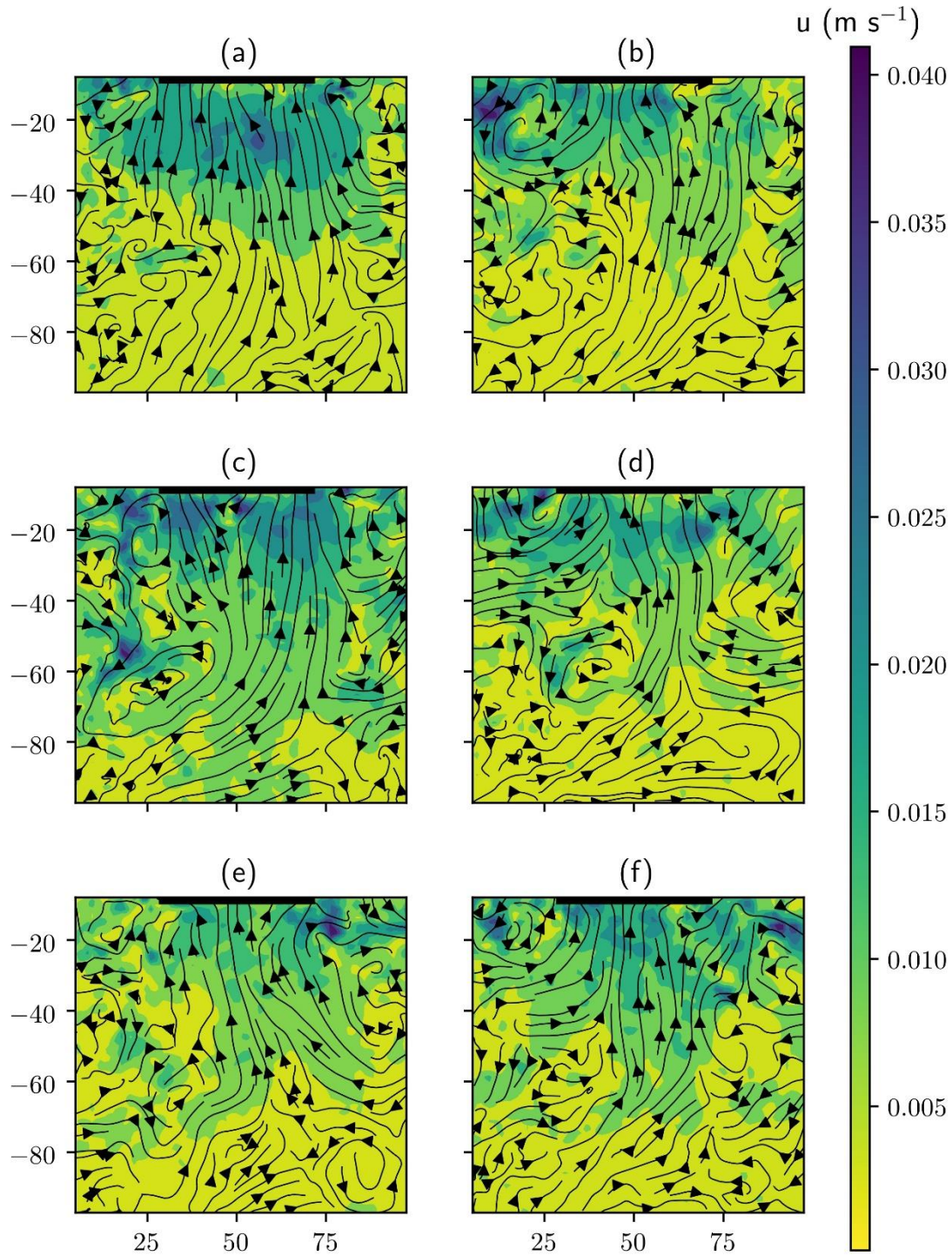


Figure 4: Transient velocity measurements from the PIV experiment showing spatial distribution of average acoustic flow structures at 50% sonotrode power. The above snapshots correspond to intervals of around 2 s. The thick line at the top represents the sonotrode surface.

Figure 5 illustrates the predicted flow pattern as a function of bubble volume fraction, with velocities averaged over 10 s and 20 s of simulation time. This relatively large time simulation time is required at low powers to ensure that the solution for the acoustic streaming pattern is compatible with the time-averaged approach also applied to the PIV data. The whole 2D domain is presented in these results. The hatched rectangle at the top of the contours represents the sonotrode. The dotted

rectangular window represents the PIV windows in which direct comparison with the experiments is possible. The left contours represent velocities while the right contours represent the flow pressure p . The flow direction is represented using streamlines overlaid on the pressure contours.

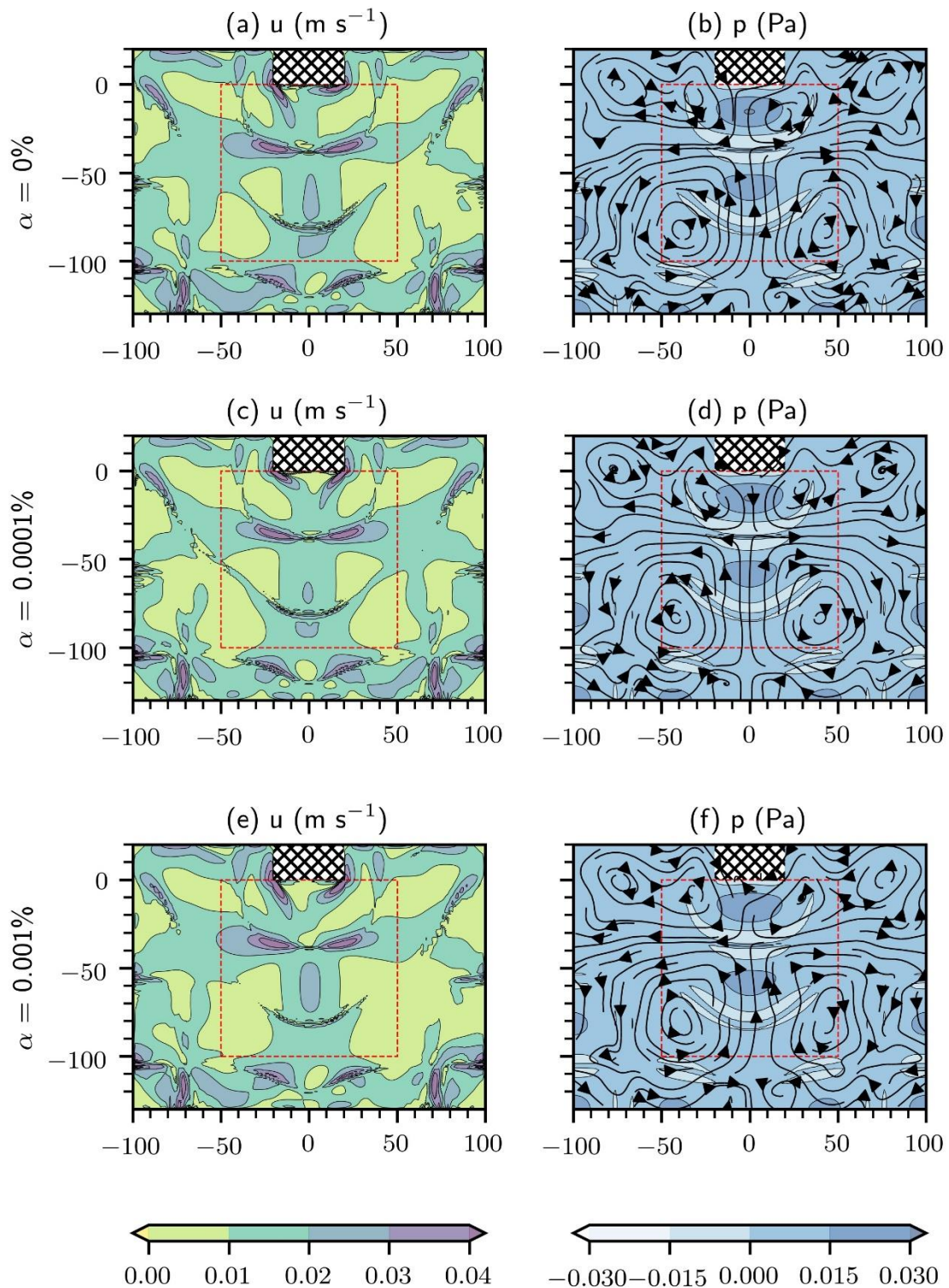


Figure 5: (Left) Velocity contours along the xy axis and (Right) velocity streamlines and flow pressure contours from simulations corresponding to water experiments at 50 % sonotrode power as a function of assumed bubble fraction. The fields are averaged from the results between 10 s and 20 s of simulation time. The dotted centre box corresponds to the PIV window. Dimensions are in mm.

The change in bubble volume fraction in the code was implemented by setting different values of bubble number densities N_0 in equation (11). The results in Figure 5 show a strong dependence on the predicted acoustic pattern on the bubble fraction in the computational domain. Bubble volume fractions $\alpha < 0.01\%$ gave good qualitative agreement with the experiment, with a maximum velocity of 0.04 m s^{-1} below the sonotrode surface, a net upflow along the sonotrode axis, and turbulent recirculation at the sides. The location of the maximum velocity is predicted to be slightly lower than the experiments, but the maximum is of the correct order of magnitude. At larger bubble volume fractions $\alpha > 0.01\%$, the numerical simulations became unstable and diverged to unrealistic solutions: these velocities are not presented here. These results demonstrate one shortcoming of the model: the large sensitivity of the model to bubble number density.

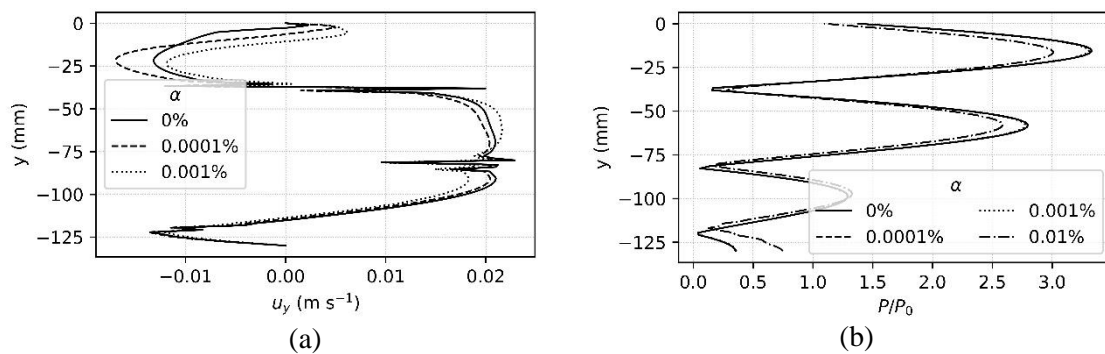


Figure 6: (a) y-component of velocity and (b) acoustic pressure along the axis of the sonotrode from simulations corresponding to water with the transducer at 50% power as a function of bubble volume fraction averaged between 10 s and 20 s of simulation time. Positive velocities represent upflow. Note that the peaks in the predicted y components of velocity correspond to corresponding regions of high acoustic pressure gradients: these peaks are predicted because the driving force f from equation 14 is computed from acoustic pressure gradients.

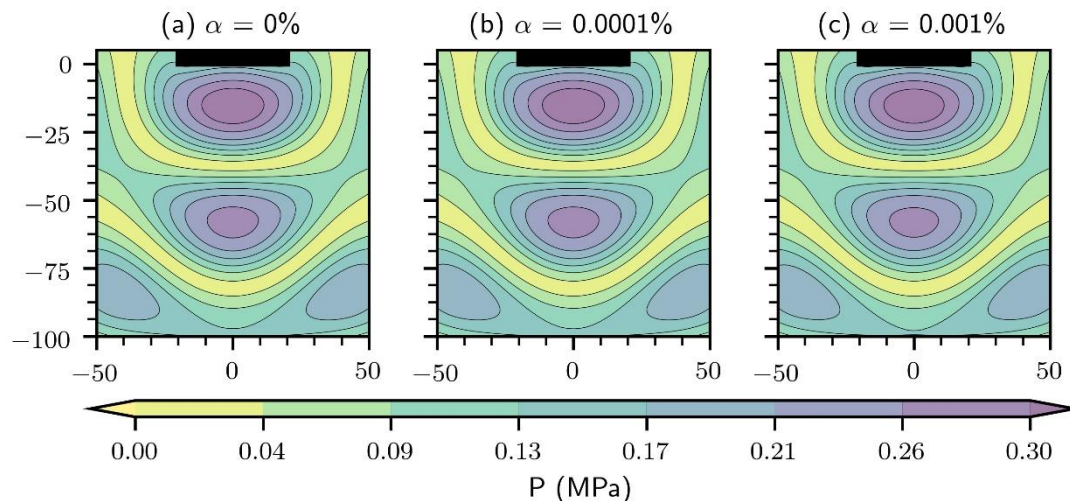


Figure 7: Acoustic pressure contours from simulation corresponding to water experiments at 50% sonotrode power averaged between 10 s and 20 s of simulation time. Dimensions are in mm. The thick line at the top represents the sonotrode surface.

The flow direction can be understood by the flow pressure pattern: zones of low pressure are predicted in the middle of the PIV window, i.e. 40 mm below the surface of the sonotrode, and the flow is forced towards these zones from the bottom of the tank. There is also a predicted net low

(flow) pressure zone just under the sonotrode (located 40 mm below the sonotrode surface) as indicated by the white contours in Figure 5 (right) explaining why the net flow below the sonotrode is upwards. However, a high-pressure zone also pushes some flow down between 20–35 mm below the sonotrode: this was not observed in the experiments and is a short-coming of this 2D model. This infers a competition between the in the vicinity high and low-pressure zones that regulate the flow direction.

At $\alpha < 0.01\%$, the acoustic pressure pattern did not deviate significantly from predictions of the linear Helmholtz equation, as shown in Figure 6(b) and Figure 7. The pressure pattern was almost identical to that without bubbles i.e. $\alpha = 0\%$. There is a slight difference between Figures 7 (a), (b), and (c): this is better visualized in Figure 6(b). The three lines do not perfectly overlap in the pressure line plot, but the difference is very low compared with $\alpha = 0.01\%$. However, increasing the bubble density to $\alpha = 0.01\%$ slightly suppressed the pressure field, as shown in Figure 6(b). While the acoustic pressure solver is still robust and forces a 'converged' solution to a pressure profile, the increase in acoustic dissipation results in lower predicted acoustic pressures, but these lead to larger source terms in the momentum equation, thereby making the solver unstable.

Acoustic streaming pattern at 100 % sonotrode power

Figure 8 shows 6 PIV flow measurements from the water experiment at 100 % sonotrode power. The net flow recorded is always downwards. Figure 9 and Figure 10 (a) show the corresponding time-averaged velocity predictions with a sonotrode amplitude of $8.5\ \mu\text{m}$ (null-peak). Doubling the amplitude resulted in a net downward flow for all bubble fractions. The cases with $\alpha < 0.01\%$ show good agreement with the PIV measurements in Figure 3 (b). The flow pattern consists of a strong downwards jet with a maximum velocity of $0.24\ \text{m s}^{-1}$, with the same order of magnitude as the recorded net maximum velocities. The time evolution of one such predicted structure for the case of $\alpha = 0.001\%$ is shown in Figure 11. Recirculations were present at the side of the axial jet, and there the conical flow pattern was established just below the sonotrode. Increasing the bubble density further resulted in chaotic, fluctuating flow patterns that indicate numerical divergence.

Note that the net downflow can be explained by the large high pressure zone sandwiched between the low pressure zones at around 40 mm below the sonotrode. This large relative flow pressure value is not present in the 50 % sonotrode case and prevents the net upflow from the bottom of the tank and forces the liquid down, consistent with what is observed in the PIV experiments. As in the water experiment at 50 % sonotrode power, large kinks in velocity appear in corresponding large pressure gradient regions.

The acoustic pressure patterns showed a large deviation from linear (Helmholtz) predictions as the bubble fraction increased, as shown in Figure 10(b) and Figure 12. For $\alpha = 0.01\%$, the acoustic pressures were no longer accurately described by a linear Helmholtz equation and the non-linear terms became dominant. This demonstrates the need for accurate non-linear pressure models to study acoustic cavitation adequately at high forcing amplitudes in the presence of a large fraction of bubbles.

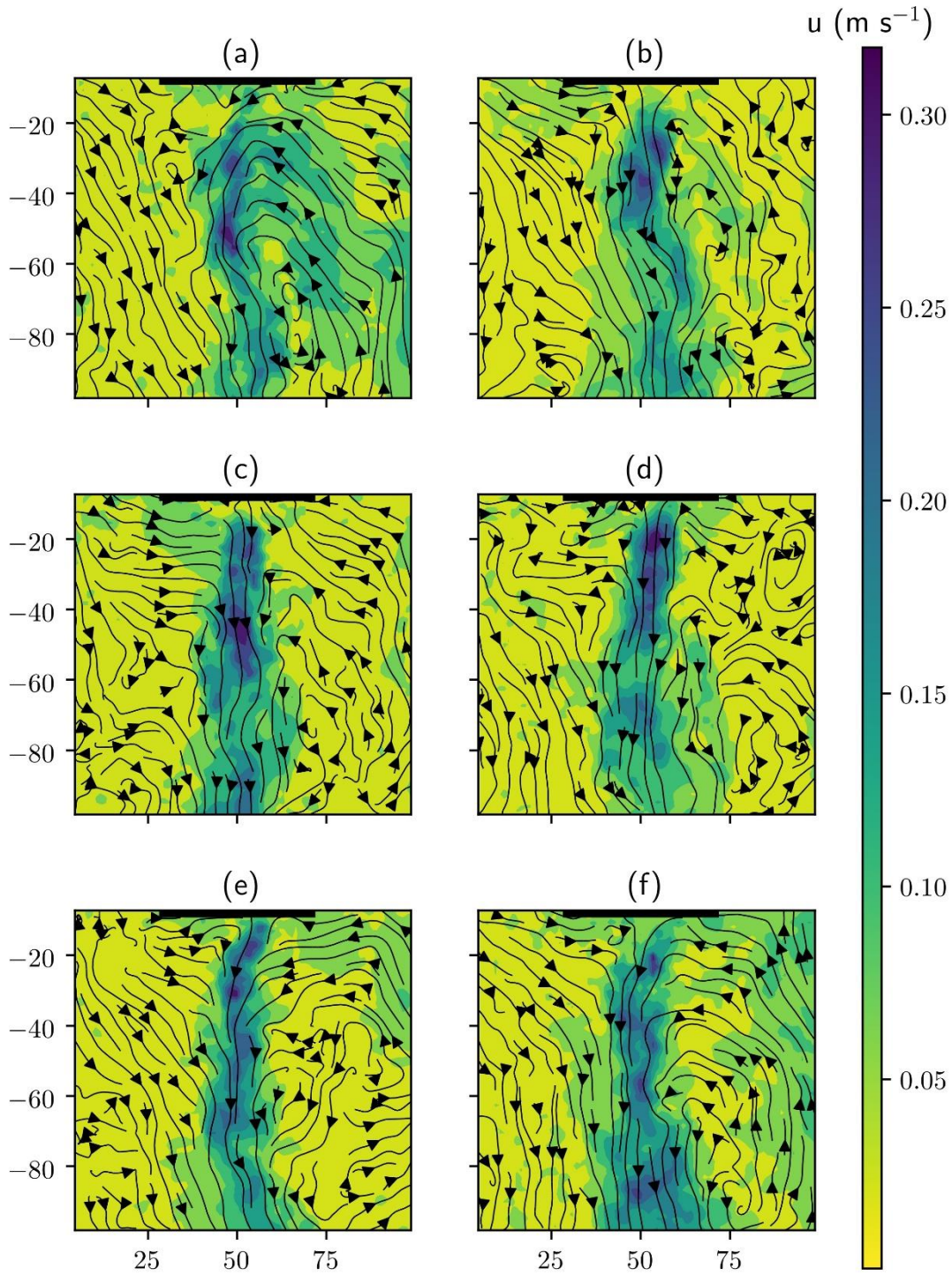


Figure 8: Transient velocity measurements from the PIV experiment showing spatial distribution of average acoustic flow structures at 100% sonotrode power. The above snapshots correspond to intervals of around 1 second. The thick line at the top represents the sonotrode surface.

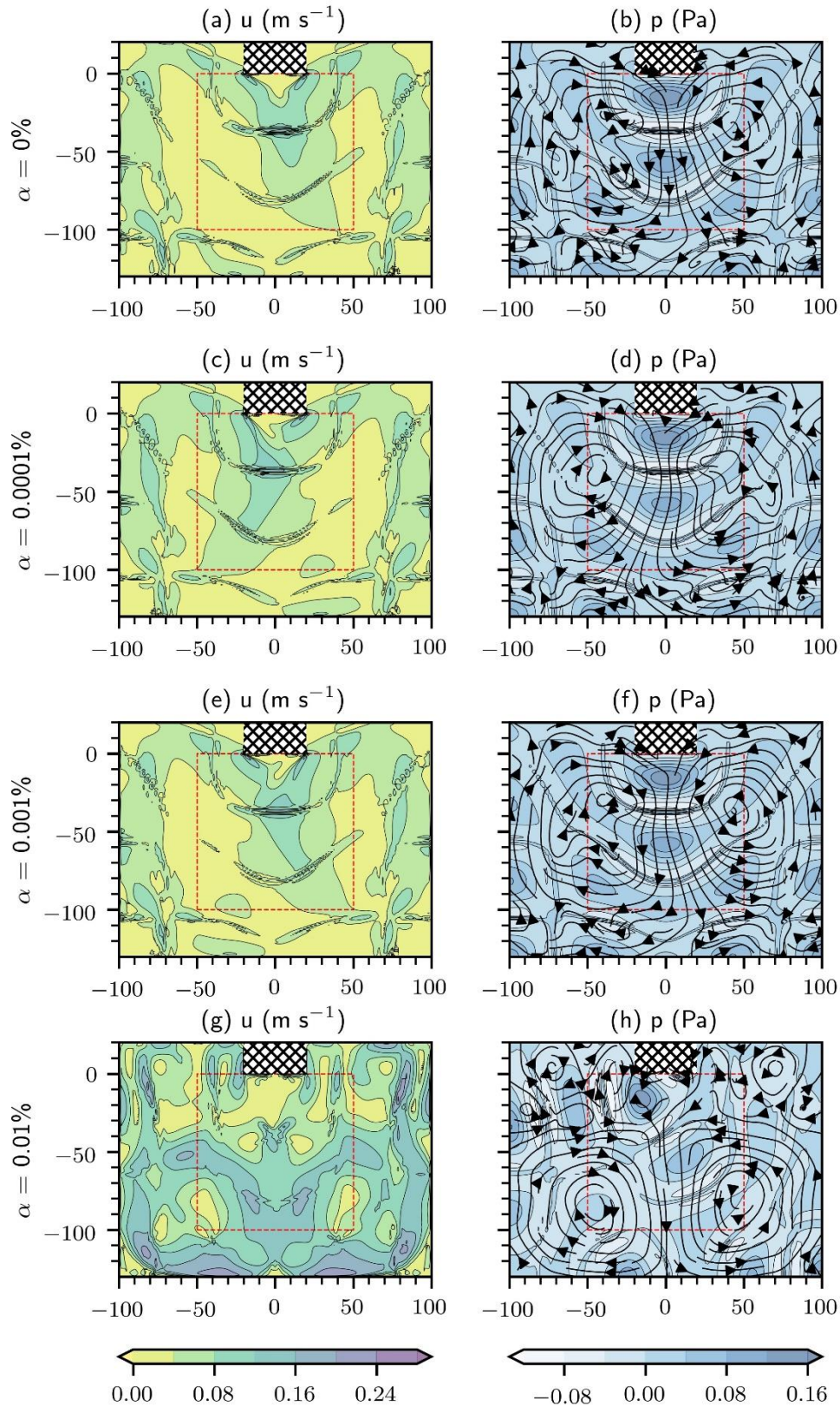


Figure 9: Velocity contours, velocity streamlines, and flow pressure contours from simulation corresponding to water experiments at 100% sonotrode power averaged between 10 s and 20 s of simulation time. Dimensions are in mm.

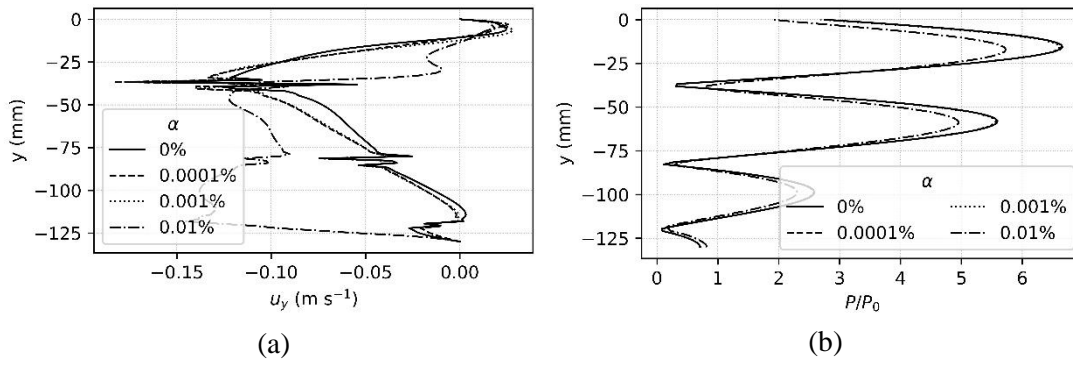


Figure 10: (a) y-component of velocity and (b) acoustic pressure along the axis of the sonotrode from simulation corresponding to water with the transducer at 100 % power as a function of bubble volume fraction averaged between 10 s and 20 s of simulation time. Positive velocities represent upflow.

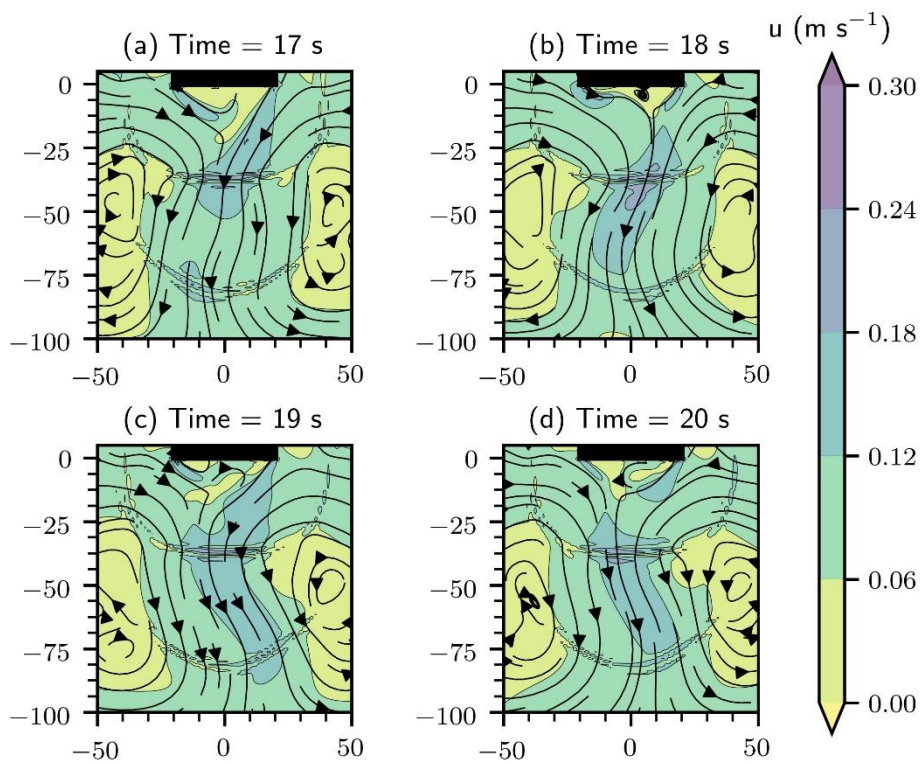


Figure 11: Time evolution of contours and streamlines from the simulation corresponding to water experiments at 100 % sonotrode power for $\alpha = 0.001\%$. Dimensions are in mm. The thick line at the top represents the sonotrode surface.

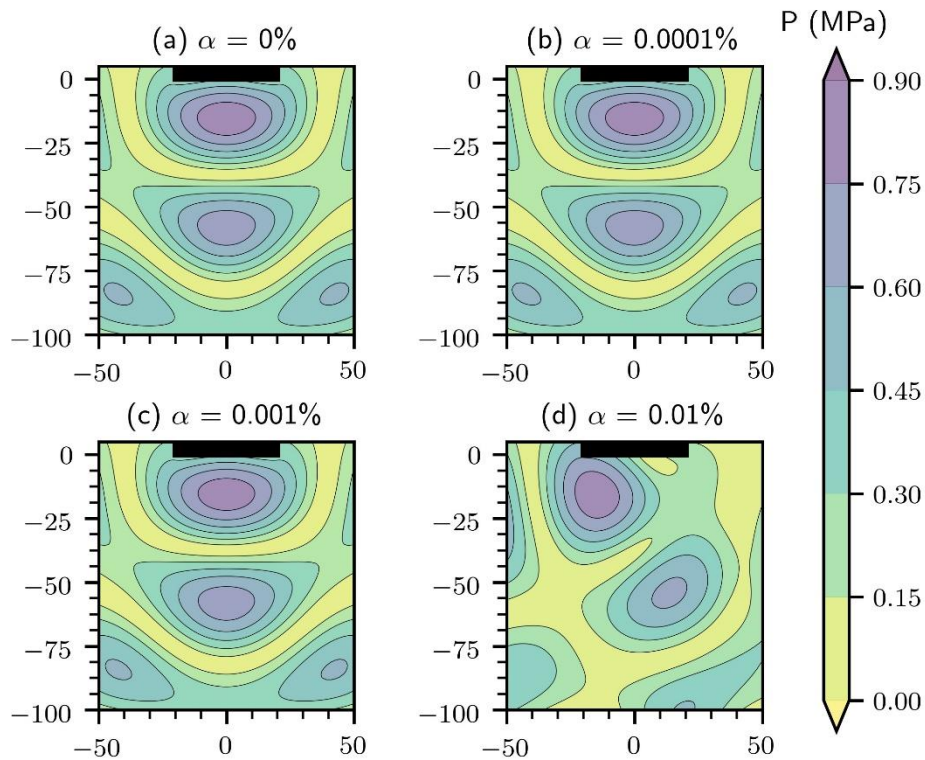


Figure 12: Acoustic pressure contours from simulation corresponding to water experiments at 100 % sonotrode power averaged between 10 s and 20 s of simulation time. Dimensions are in mm. The thick line at the top represents the sonotrode surface.

Application of the model to the ultrasonic treatment of molten aluminium

The changes in acoustic streaming pattern due to the presence of bubbles are now investigated by application of the model for the case of the ultrasonic processing of liquid aluminium. The simulations are repeated using the same conditions as the water tank simulations at 50 % sonotrode power, but with the liquid replaced by molten aluminium, mimicking the treatment of the alloy just prior to casting and solidification. At low bubble fractions, the results were similar to those of water: a net upward flow along the axis of the sonotrode. On increasing the bubble fraction to larger values, the flow begins to reverse as shown in Figure 13 (h). This effect is also demonstrated in the line plot of the melt y-velocity in Figure 14 (a).

Figure 14 (b) and Figure 15 illustrate the acoustic pressure profile for molten aluminium. At lower bubble fractions, the non-linear contribution to the pressure equation was small and did not affect the acoustic pressure predictions significantly, but pressure was significantly increased as the bubble fraction increased.

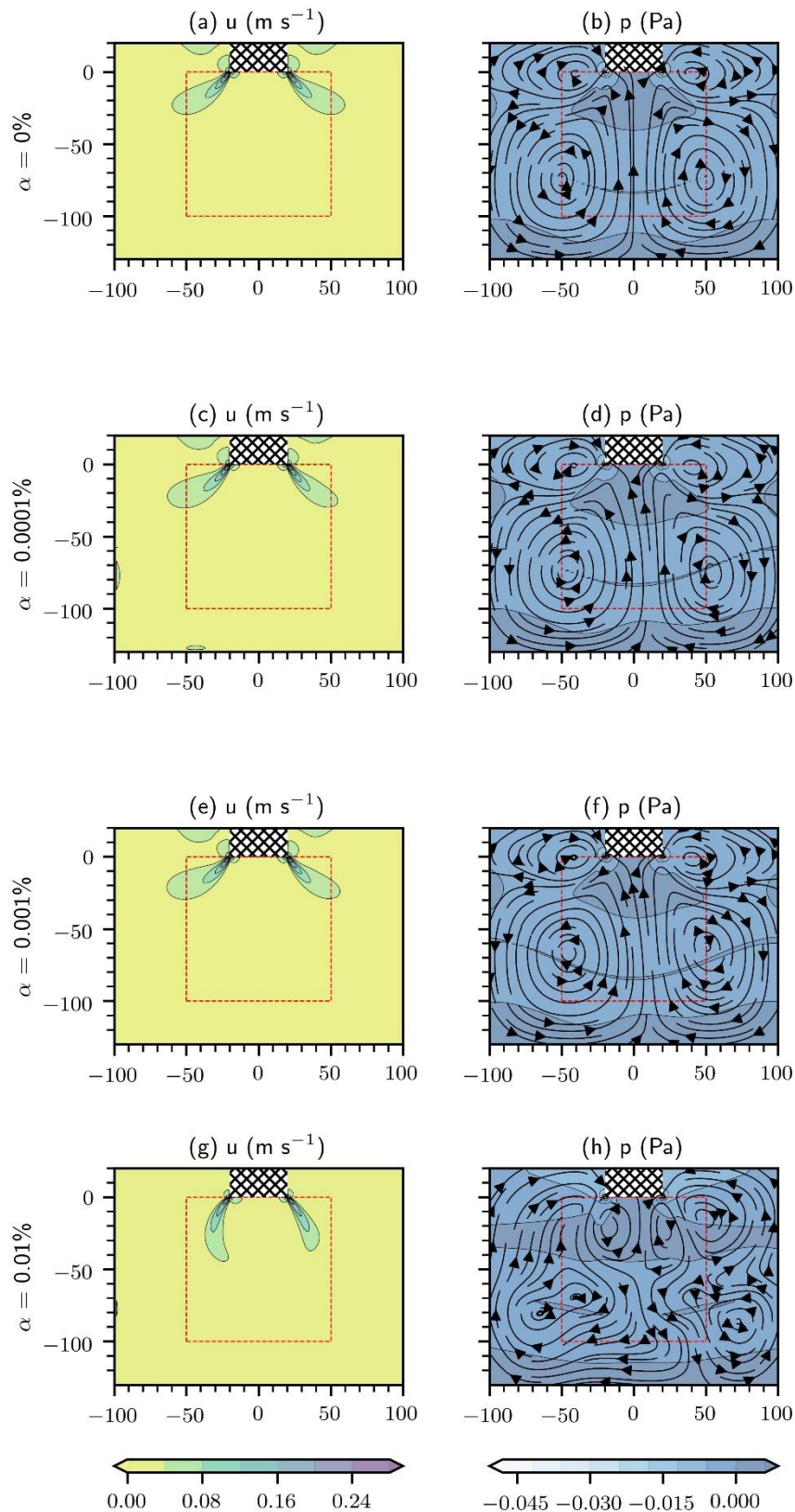


Figure 13: (Left) Velocity contours and (Right) velocity streamlines and hydrodynamic pressure contours from simulations corresponding to aluminium experiments at 50 % sonotrode power as a function of assumed bubble fraction. The fields are averaged from the results between 10 s and 20 s of simulation time. The dotted centre box corresponds to the PIV window. Dimensions are in mm.

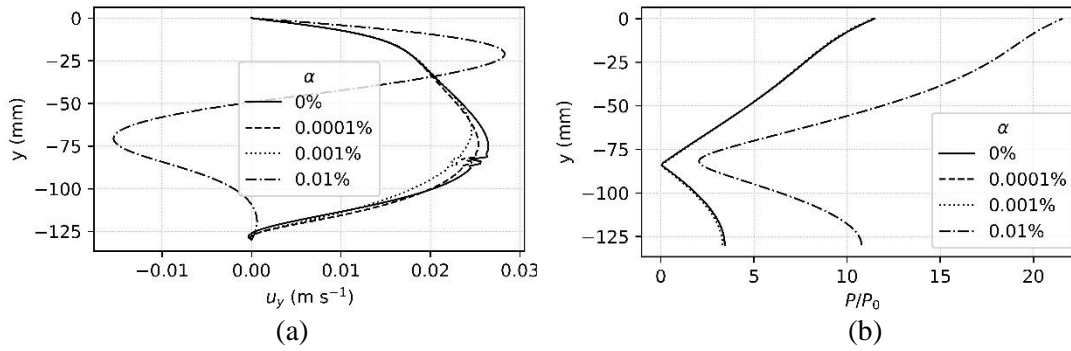


Figure 14: (a) y-component of velocity and (b) acoustic pressure along the axis of the sonotrode from simulation corresponding to liquid aluminium treated at 50 % sonotrode power as a function of bubble volume fraction averaged between 10 s and 20 s of simulation time. Positive velocities represent upflow.

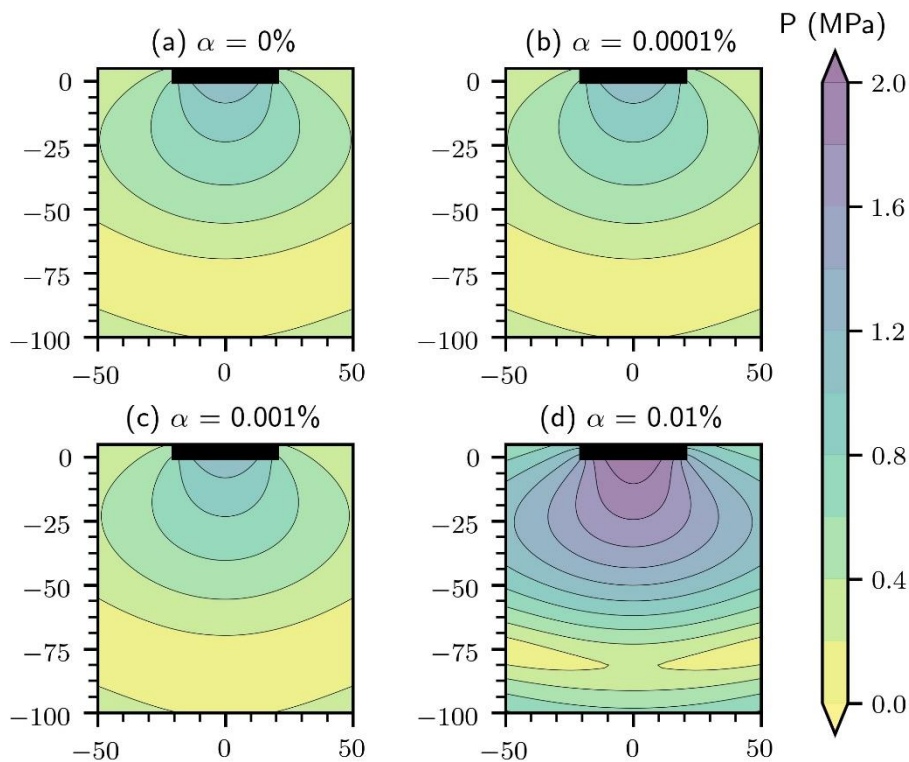


Figure 15: Acoustic pressure contours from simulation corresponding to liquid aluminium treated at 50 % sonotrode power averaged between 10 s and 20 s of simulation time. Dimensions are in mm. The thick line at the top represents the sonotrode surface.

The results in aluminium also demonstrate competing interplays in the flow profile inside the melt. On one hand, large pressures are generally considered to be required to de-agglomerate particle clusters inside the bulk [1,43]. However, according to the results here, these large pressures are accompanied by a strong induced downflow that pushes melt away from the sonotrode and the active cavitation zone, and higher velocities that will reduce the residence time of liquid in the energetic zone close to the sonotrode tip. Upward flow, at lower power, below the sonotrode could be attractive in this regard to extend the melt residence time in the cavitation zone. Also, operating at lower power and velocity may help preserve the integrity of the free, top surface of the liquid, which is known to be critical if entrainment of surface oxide [44], which always forms on liquid

aluminium, into the bulk of the melt is to be minimised. If ultrasonic processing were applied to the melt sump in direct chill casting of aluminium alloys (that typically contain zinc, copper and/or magnesium) [45], the results of either upward or downward flow on the final microstructure and macrosegregation might be investigated, noting that downflow would “push” hot, relatively dilute liquid down the billet centreline quickly, while upward flow would “suck” relatively cool, more concentrated liquid toward the melt bulk more slowly. The effects on the final grain structure and distribution of alloying elements under these conditions are difficult to predict, but tuning between upward and downward flow may add an extra degree of freedom to industrial practice and the range of final structures that might be contrived.

Conclusions

Acoustic streaming in water has been predicted using Louisnard’s non-linear propagation model [26] coupled with transient Reynold-Averaged Navier-Stokes equations, closed with the $k-\omega$ SST model. The coupled set of equations have been solved stably using a finite volume method and the results compare favourably with velocity vector fields measured by particular image velocimetry in water at two ultrasonic powers (at 50 % and 100% of available sonotrode power).

A net upward flow on the model centreline was predicted at low sonication power and observed by experiment, which has previously been difficult to predict accurately because the effect of cavitation on the acoustic streaming pattern has been neglected. The model shows a high sensitivity of the acoustic flow pattern (both in magnitude and direction) to the cavitation bubble volume fraction α , which is implicated as a critical parameter for useful model predictions.

The model was subsequently applied to liquid aluminium to achieve the prediction of acoustic streaming that considers the effect of cavitating bubbles for the first time. Low bubble volume fractions at low sonication power result in an upward centreline flow, which may be attractive in processing liquid metal in continuous processes. The availability of either upward or downward centreline flow by model and experiment according to sonotrode power may introduce additional useful flexibility on how ultrasonic processing may be applied to liquid metal processing during casting, and in other sono-technologies.

Acknowledgements

Financial support from the UK Engineering and Physical Sciences Research Council (EPSRC) through grants LiME Hub (EP/N007638/1) and UltraMelt2 (EP/R011001/1, EP/R011044/1, and EP/R011095/1) is gratefully acknowledged.

Data availability statement

The processed data required to reproduce these findings are available to download from <https://dx.doi.org/10.17633/rd.brunel.7435457>

References

- [1] D.G. Eskin, I. Tzanakis, F. Wang, G.S.B. Lebon, K. Pericleous, P.D. Lee, T. Connolley, J. Mi, Fundamental studies of ultrasonic melt processing, in: Proc. 6th Decenn. Int. Conf. Solidif. Process., Old Windsor, UK, 2017: pp. 546–549.
- [2] O.V. Abramov, Action of high intensity ultrasound on solidifying metal, *Ultrasonics*. 25 (1987) 73–82. doi:10.1016/0041-624X(87)90063-1.
- [3] J. Campbell, Effects of vibration during solidification, *Int. Met. Rev.* 26 (1981) 71–108. doi:10.1179/imtr.1981.26.1.71.
- [4] G.I. Eskin, D.G. Eskin, *Ultrasonic treatment of light alloy melts*, Second edition, Taylor & Francis, CRC Press, Boca Raton, 2015.
- [5] G.. Eskin, Cavitation mechanism of ultrasonic melt degassing, *Ultrason. Sonochem.* 2 (1995) S137–S141. doi:10.1016/1350-4177(95)00020-7.
- [6] S. Komarov, K. Oda, Y. Ishiwata, N. Dezhkunov, Characterization of acoustic cavitation in water and molten aluminum alloy, *Ultrason. Sonochem.* 20 (2013) 754–761. doi:10.1016/j.ultsonch.2012.10.006.
- [7] G. Wang, P. Croaker, M. Dargusch, D. McGuckin, D. StJohn, Simulation of convective flow and thermal conditions during ultrasonic treatment of an Al-2Cu alloy, *Comput. Mater. Sci.* 134 (2017) 116–125. doi:10.1016/j.commatsci.2017.03.041.
- [8] D. Shu, B. Sun, J. Mi, P.S. Grant, A High-Speed Imaging and Modeling Study of Dendrite Fragmentation Caused by Ultrasonic Cavitation, *Metall. Mater. Trans. A*. 43 (2012) 3755–3766. doi:10.1007/s11661-012-1188-3.
- [9] I. Tzanakis, W.W. Xu, D.G. Eskin, P.D. Lee, N. Kotsovinos, In situ observation and analysis of ultrasonic capillary effect in molten aluminium, *Ultrason. Sonochem.* 27 (2015) 72–80. doi:10.1016/j.ultsonch.2015.04.029.
- [10] I. Tudela, V. Sáez, M.D. Esclapez, M.I. Díez-García, P. Bonete, J. González-García, Simulation of the spatial distribution of the acoustic pressure in sonochemical reactors with numerical methods: A review, *Ultrason. Sonochem.* 21 (2014) 909–919. doi:10.1016/j.ultsonch.2013.11.012.
- [11] O. Louisnard, A viable method to predict acoustic streaming in presence of cavitation, *Ultrason. Sonochem.* 35 (2017) 518–524. doi:10.1016/j.ultsonch.2016.09.013.
- [12] L. Nastac, Mathematical Modeling of the Solidification Structure Evolution in the Presence of Ultrasonic Stirring, *Metall. Mater. Trans. B*. 42 (2011) 1297–1305. doi:10.1007/s11663-011-9539-9.
- [13] A.K. Singhal, M.M. Athavale, H. Li, Y. Jiang, Mathematical Basis and Validation of the Full Cavitation Model, *J. Fluids Eng.* 124 (2002) 617. doi:10.1115/1.1486223.
- [14] G.S.B. Lebon, I. Tzanakis, G. Djambazov, K. Pericleous, D.G. Eskin, Numerical modelling of ultrasonic waves in a bubbly Newtonian liquid using a high-order acoustic cavitation model, *Ultrason. Sonochem.* 37 (2017) 660–668. doi:10.1016/j.ultsonch.2017.02.031.
- [15] G.S.B. Lebon, I. Tzanakis, K. Pericleous, D. Eskin, Experimental and numerical investigation of acoustic pressures in different liquids, *Ultrason. Sonochem.* 42 (2018) 411–421. doi:10.1016/j.ultsonch.2017.12.002.
- [16] L.V. Wijngaarden, On the equations of motion for mixtures of liquid and gas bubbles, *J. Fluid Mech.* 33 (1968) 465. doi:10.1017/S002211206800145X.
- [17] R.E. Caflisch, M.J. Miksis, G.C. Papanicolaou, L. Ting, Effective equations for wave propagation in bubbly liquids, *J. Fluid Mech.* 153 (1985) 259. doi:10.1017/S0022112085001252.
- [18] C. Vanhille, C. Campos-Pozuelo, Nonlinear Ultrasonic Propagation in Bubbly Liquids: A Numerical Model, *Ultrasound Med. Biol.* 34 (2008) 792–808. doi:10.1016/j.ultrasmedbio.2007.11.004.
- [19] D. Fuster, T. Colonius, Modelling bubble clusters in compressible liquids, *J. Fluid Mech.* 688 (2011) 352–389. doi:10.1017/jfm.2011.380.

- [20] M.C. Schenker, M.J.B.M. Pourquié, D.G. Eskin, B.J. Boersma, PIV quantification of the flow induced by an ultrasonic horn and numerical modeling of the flow and related processing times, *Ultrason. Sonochem.* 20 (2013) 502–509. doi:10.1016/j.ultsonch.2012.04.014.
- [21] M. Barthès, G. Mazue, D. Bonnet, R. Viennet, J.-Y. Hihn, Y. Bailly, Characterization of the activity of ultrasound emitted in a perpendicular liquid flow using Particle Image Velocimetry (PIV) and electrochemical mass transfer measurements, *Ultrasonics*. 59 (2015) 72–78. doi:10.1016/j.ultras.2015.01.015.
- [22] X. Ma, B. Huang, G. Wang, M. Zhang, Experimental investigation of conical bubble structure and acoustic flow structure in ultrasonic field, *Ultrason. Sonochem.* 34 (2017) 164–172. doi:10.1016/j.ultsonch.2016.05.027.
- [23] F. Wang, D. Eskin, J. Mi, C. Wang, B. Koe, A. King, C. Reinhard, T. Connolley, A synchrotron X-radiography study of the fragmentation and refinement of primary intermetallic particles in an Al-35 Cu alloy induced by ultrasonic melt processing, *Acta Mater.* 141 (2017) 142–153. doi:10.1016/j.actamat.2017.09.010.
- [24] W. Mirihanage, W. Xu, J. Tamayo-Ariztondo, D. Eskin, M. Garcia-Fernandez, P. Srirangam, P. Lee, Synchrotron radiographic studies of ultrasonic melt processing of metal matrix nano composites, *Mater. Lett.* 164 (2016) 484–487. doi:10.1016/j.matlet.2015.11.022.
- [25] B. Wang, D. Tan, T.L. Lee, J.C. Khong, F. Wang, D. Eskin, T. Connolley, K. Fezzaa, J. Mi, Ultrafast synchrotron X-ray imaging studies of microstructure fragmentation in solidification under ultrasound, *Acta Mater.* 144 (2018) 505–515. doi:10.1016/j.actamat.2017.10.067.
- [26] O. Louisnard, A simple model of ultrasound propagation in a cavitating liquid. Part I: Theory, nonlinear attenuation and traveling wave generation, *Ultrason. Sonochem.* 19 (2012) 56–65. doi:10.1016/j.ultsonch.2011.06.007.
- [27] O. Louisnard, A simple model of ultrasound propagation in a cavitating liquid. Part II: Primary Bjerknes force and bubble structures, *Ultrason. Sonochem.* 19 (2012) 66–76. doi:10.1016/j.ultsonch.2011.06.008.
- [28] H. Dogan, V. Popov, Numerical simulation of the nonlinear ultrasonic pressure wave propagation in a cavitating bubbly liquid inside a sonochemical reactor, *Ultrason. Sonochem.* 30 (2016) 87–97. doi:10.1016/j.ultsonch.2015.11.011.
- [29] F.J. Trujillo, A strict formulation of a nonlinear Helmholtz equation for the propagation of sound in bubbly liquids. Part I: Theory and validation at low acoustic pressure amplitudes, *Ultrason. Sonochem.* 47 (2018) 75–98. doi:10.1016/j.ultsonch.2018.04.014.
- [30] H.G. Weller, OpenFOAM, OpenCFD Ltd (ESI Group), 2018.
- [31] I. Tzanakis, G.S.B. Lebon, D.G. Eskin, K.A. Pericleous, Characterizing the cavitation development and acoustic spectrum in various liquids, *Ultrason. Sonochem.* 34 (2017) 651–662. doi:10.1016/j.ultsonch.2016.06.034.
- [32] Lord Rayleigh, VIII. *On the pressure developed in a liquid during the collapse of a spherical cavity*, Lond. Edinb. Dublin Philos. Mag. J. Sci. 34 (1917) 94–98. doi:10.1080/14786440808635681.
- [33] M.S. Plesset, The dynamics of cavitation bubbles, *J. Appl. Mech.* 16 (1949) 277–282.
- [34] A. Prosperetti, L.A. Crum, K.W. Commander, Nonlinear bubble dynamics, *J. Acoust. Soc. Am.* 83 (1988) 502–514. doi:10.1121/1.396145.
- [35] K.W. Commander, A. Prosperetti, Linear pressure waves in bubbly liquids: Comparison between theory and experiments, *J. Acoust. Soc. Am.* 85 (1989) 732–746. doi:10.1121/1.397599.
- [36] F.R. Menter, M. Kuntz, R. Langtry, Ten Years of Industrial Experience with the SST Turbulence Model, in: *Turbul. Heat Mass Transf.* 4, Begell House, Antalya, Turkey, 2003: pp. 625–632.
- [37] I. Tzanakis, G.S.B. Lebon, D. Eskin, M. Hyde, P.S. Grant, Investigation of acoustic streaming and cavitation intensity in water as an analogue for liquid metal, in: *Proc. 10th Int. Symp. Cavitation CAV2018*, Baltimore, Maryland, USA, 2018.
- [38] I. Tzanakis, M. Hodnett, G.S.B. Lebon, N. Dezhkunov, D.G. Eskin, Calibration and performance assessment of an innovative high-temperature cavitometer, *Sens. Actuators Phys.* 240 (2016) 57–69. doi:10.1016/j.sna.2016.01.024.

- [39] R.. Issa, Solution of the implicitly discretised fluid flow equations by operator-splitting, *J. Comput. Phys.* 62 (1986) 40–65. doi:10.1016/0021-9991(86)90099-9.
- [40] F. Menter, T. Esch, Elements of industrial heat transfer predictions, in: *Proc. 16th Braz. Congr. Mech. Eng., Uberlândia, Brazil, 2001*: pp. 117–127.
- [41] J. Smagorinsky, General circulation experiments with the primitive equations: I. The basic experiment, *Mon. Weather Rev.* 91 (1963) 99–164. doi:10.1175/1520-0493(1963)091<0099:GCEWTP>2.3.CO;2.
- [42] A. Yoshizawa, Statistical theory for compressible turbulent shear flows, with the application to subgrid modeling, *Phys. Fluids.* 29 (1986) 2152. doi:10.1063/1.865552.
- [43] A. Manoylov, B. Lebon, G. Djambazov, K. Pericleous, Coupling of Acoustic Cavitation with Dem-Based Particle Solvers for Modeling De-agglomeration of Particle Clusters in Liquid Metals, *Metall. Mater. Trans. A.* 48 (2017) 5616–5627. doi:10.1007/s11661-017-4321-5.
- [44] J. Campbell, Entrainment defects, *Mater. Sci. Technol.* 22 (2006) 127–145. doi:10.1179/174328406X74248.
- [45] J.H. Grandfield, D.G. Eskin, I.F. Bainbridge, *Direct-Chill Casting of Light Alloys: Science and Technology*, John Wiley & Sons, Hoboken, NJ, 2013.